Research paper

Ignition delay, erosive burning and other animals – Lessons learnt about transient phenomena

Jonathan Sivan*†, Yair Solomon*, and Oren Peles*

*IMI Systems, Ramat Ha-Sharon, 4711001, ISRAEL
Phone: +97-22544327685
†Corresponding author: jonathan.sivan@imisystems.com

Received: March 8, 2018 Accepted: March 15, 2019

Abstract

Transient phenomena during combustion of solid rocket motors (SRMs) are not always accounted for during development, but can cause havoc if neglected. Most ballistic codes tend to simulate SRM operation at quasi-steady state conditions, thus giving good prediction of large time scale events, but ignoring local perturbations. At IMI systems special thought has been given to understanding transient phenomena occurring mainly at the beginning of motor operations. Through reduction of static test firing data of several motors, as well as specifically built experimental tools, we focused on two common transient phenomena: erosive burning and ignition transient. The combination of both phenomena can cause different behaviours during the initial phase of SRM operation. In this work we will demonstrate our attempt to interpret test results from high volume loaded SRMs with different ignition systems. We will also show our modelling of such systems using 1D quasi-steady state ballistic code as well as 3D CFD Navier-Stokes solvers. We validate the simulation with test results.

Keywords: ignition delay, erosive burning, aft igniter

1. Introduction

IMI Systems is a company which produces solid propulsion systems. In recent years we have invested much research to address the problems in predicting the ignition phase of solid rocket motors (SRMs). In this paper we hope to share some of our insight regarding the cause of prediction inaccuracies during this stage, as well as address some of the ways to overcome these issues. This work is a combination of observations, experimental research and theoretical work done during the past decade.

Solid rocket motors (SRMs) produce a relatively well defined repeatable thrust vs. time profile. This profile cannot be changed ad hoc by control, as opposed to other propulsion systems[1]. Therefore, robustness and repeatability of the SRM is a crucial design parameter of the whole propulsion system. Knowledge of how to predict and simulate the thrust profile under various operating conditions is the basis of any well designed SRM. Inability to correctly predict the thrust profile, or at the very least identify points at which a large uncertainty exists, will lead to a control system that needs to deal with a larger tolerance than it was designed for. This can lead to unexpected development and redevelopment phases, and a substantial increase in non-recurring engineering cost to the project.

The thrust of a rocket is governed by the basic thrust equation[2].

$$F = \eta C_F P_c A_t \tag{1}$$

Where F is the thrust, η is the nozzle efficiency, C_F the thrust coefficient, P_c the stagnation pressure at the motor aft and A_t the nozzle throat area. C_F, η and A_t are all parameters dependent mainly on nozzle geometry and external pressure (to a lesser degree on the internal pressure, if the pressure is high enough). P_c, the internal pressure of the motor varies in time and is dependent on the solid fuel composition and shape.

A common practice to calculate P_c is to assume a quasi-steady-state solution to the flow in the motor. Mass ejection through the nozzle (m_{dis}) is then equal to mass addition due to the combustion process (m_{add}):

$$\dot{m}_{dis} = \frac{P_c A_t g}{C^*} \tag{2}$$

$$\dot{m}_{add} = r \rho_p A_b \tag{3}$$

Where g is the gravity constant, C^* is the characteristic velocity (a parameter associated with propellant composition's energy). r is the propellant burning rate (linear regression rate of the propellant surface), ρ_p is the solid propellant density and A_b the total burning area of the propellant surface. Equation (3) assumes that the burning rate is uniform throughout the motor (which is not generally the case). By equating (2) and (3) and assuming a power law dependence of burning rate on pressure (commonly referred to as Vielle law): $r = a^* P^n$, one can calculate the motor pressure (also assumed uniform) in the motor.

$$P_c = \left(\frac{A_b(t) \rho_p C^* a}{A_t(t)} \right)^{\frac{1}{1-n}} \tag{4}$$

In Equation (4) the variables that are dependent on time have been explicitly marked. By substituting (4) into (1) a good estimate of thrust vs. time can be established, provided that the burning area of the propellant surface is known or can be computed at each time. Since calculating the burning area is a geometric problem it is considered trivial, although in practice it can be just as challenging as calculating the flow. An example of propellant burn lines for a simple case can be seen in Figure 1.

In some applications this simple procedure to determine thrust profile is quite adequate. Indeed, in almost all cases Equation (1) and (4) can be used with a very high degree of accuracy after sufficient time has passed (dependent on the propellant grain geometry and nozzle throat area). However, Equation (3) and (4) are based on rather strong assumptions that are not generally applicable:

1) Pressure is constant throughout the motor — this is not the case and is a poor estimation when high velocity fields are present inside the motor. Such velocities develop in cases where motors are highly loaded (the percent of fuel relative to total casing volume is high). Such applications include small rockets where geometric constraints require small volumes.
2) Burning rate is only dependent on pressure — At high internal velocities it is known that burning rate increases significantly (an increase of up to 100% and even more), even though the pressure decreases[3]. This phenomenon is known as erosive burning and will be discussed further in Section 2.
3) Equation (4) assumes quasi-steady state conditions. In effect, especially during ignition, steady state conditions do not yet apply and the discharged mass is not equal to mass addition due to combustion. To emphasize this point if one assumes Equation (4) holds, the pressure of a motor should immediately reach some finite value higher than external pressure, whereas in actuality the pressure needs to build up (usually rather slowly) to reach that level.

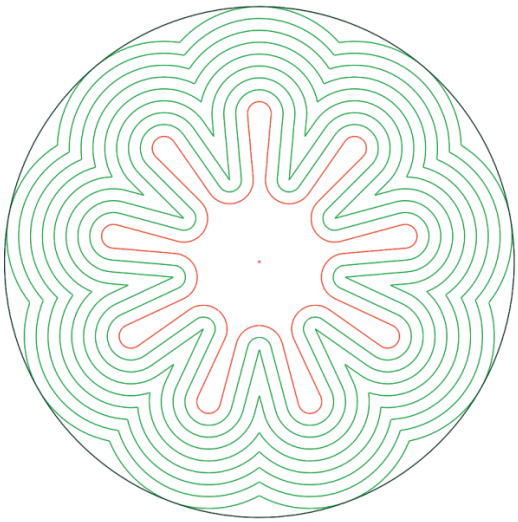

Figure 1 An example of a propellant section at different propellant regression distance. The propellant is assumed to recede an equal distance in any given section.

It is interesting to note that all of these inconsistencies occur during or close to ignition. After ignition and initial pressure build-up in the combustion chamber, changes in surface area or nozzle throat diameter are comparatively slow to characteristic volume filling/discharge times. Thus quasi-steady state can be assumed at any time (this is dependent on specific motor design but will usually be a few tens of milli-seconds up to a few hundreds of milli-seconds long). At later stages, roughly a few seconds later, propellant regression causes a large increase of port area which leads to a decrease in internal flow velocity, thus reducing pressure gradients in the motor and eliminating erosive burning.

It follows that inconsistencies and uncertainties in pressure and thrust profiles occur mainly and critically during the initial phase of combustion of a SRM. For some applications, such as small rockets, where peak pressure occurs during ignition this can be catastrophic:

1) Under-predicted pressure can result in low exit velocity of the rocket leading to extreme tip-off and a decrease of accuracy due to side-wind or even a confined fire due to failure to overcome restraining bolts (resulting in damage to the launcher).
2) Over-predicted pressure can result in casing failure due to unexpected internal pressure.
3) Sever erosive burning leads to early exposure of the casing, which can result in casing failure if the casing is exposed for a long enough period.
4) Ignition delay, caused by non-ideal ignition of the propellant surface, can be critical to missions which rely on precise timing.

The following chapters address: 1) predicting erosive burning, 2) ignition delay in motors with aft igniters. The methodology of this paper is to present the acquired data, deliver an interpretation of the results and key insights, and provide supporting computational comparisons were possible. The computational tools used in this study are our in-house quasi steady-state 1D internal ballistics software, as well a full Navier-Stokes in-house CFD solver.

An experimental apparatus was also constructed specifically to study erosive burning, and results obtained by this, as well as the basic principles of the experiments will be presented in the chapter dealing with erosive burning.

2. Erosive burning

2.1 Background

Erosive burning was first reported by Muraour[4]. It was shown that motors with a high cross-flow velocities (meaning the velocities perpendicular to ejected mass of the burning surface), tend to have an increased burning rate compared to expected Vielle law. It was later shown that the burning rate augmentation inversely correlates with burning rate, the higher the "natural" burning rate, the lower the burning rate increase due to cross-flow. Landsbaum proposed an initial rough quantitative model to explain this[5] stating that the burning rate is proportional to incoming heat flux into the propellant Q_+, and outgoing heat flux expelled from the surface Q_p:

$$r_e \propto Q_+/\rho_p Q_p \tag{5}$$

He further surmised that for most "typical" solid propellants ρ_p and Q_p are constant, so that erosive burning is mainly dependent on Q_+. This is the basis for most erosive burning models.

Most models attribute erosive burning to the following three factors:

1) Increased convective heating due to high internal cross-flow.
2) Increased turbulent flow due to high velocity of internal flow.
3) Bending of the diffusive flame closer to the propellant surface by the flow, causing increased heat flow.

In essence all models deal with increased heat flow into the propellant due to high internal velocities of the cross-flow.

Some of the most common and well known models to predict erosive are Kreidler's model[6]:

$$r = r_0\left[1+\frac{a_0}{P^{a1}}(G-G_{th})\right], G_{th} = a_2 + a_3 P^{a_n} \tag{6}$$

(Where G is the mass flux through the port area, G_{th} is a threshold value of the flux beneath which erosive burning does not exist).

Saderholm's model[7]:

$$r = \begin{cases} r_0 & M < M_{cr} \\ r_0\left(\dfrac{M}{M_{cr}}\right)^{a_0} & M_{cr} < M < 0.5 \\ r_0 a_1 (M\cdot P)^{a_2} & 0.5 < M \end{cases} \tag{7}$$

(Where M is the internal flow Mach number, M_{cr} is a threshold value of the Mach number beneath which erosive burning does not exist).

And the Lenoir-Robillard model[8]:

$$r = r_0 + \frac{\alpha G^{0.8}}{D^{0.2}}\exp\left(-a_0\frac{\rho_p r}{G}\right),$$
$$\alpha = \frac{0.0288 C_{p,g}\mu_g^{0.2} P_r^{-2/3}}{\rho_p C_{p,s}}\left(\frac{T_f - T_s}{T_s - T_{s,0}}\right) \tag{8}$$

(Where D is the hydraulic diameter of the port area, C_p is the specific heat capacity of the gas (g) and solid (s), T_f is the gas flame temperature and T_s and $T_{s,0}$ are the propellant surface temperature and core temperature respectively.)

In the above models a_i are all empirical constants, as are the critical values. They are all meant to be implemented in 1D flow codes.

Models such as Kreidler's and Saderholm's are easy to manipulate as they incorporate a great deal of empirical constants and critical parameters. However, these models are mostly empirical and are based on phenomenological observations. Lenoir and Robillard's model is based on a very basic heat transfer model (using pipe flow heat transfer correlation as a basis), and is simple to implement. In its general form α is also an empirical constant, thus enabling two degrees of freedom.

2.2 History of erosive burning at IMI systems

Erosive burning has been taken into account using internal ballistic codes ever since we first started developing highly volume loaded motors. This phenomena was first discovered to be significant in one of our early products. In Figure 2 a graph of initially predicted pressure profile vs. actual test results is shown. In the same figure a simulation incorporating Kreidler's model (with parameters taken from Equation (6)) is also shown, demonstrating how important erosive burning can be in this case.

As can be seen, a very good fit between measured and predicted results can be achieved using Kriedler's model. Lenoir and Robillard's model also gives good results, although the empirical factor alpha was adjusted to give the proper fit of initial pressure. Ignoring erosive burning results in a significantly different pressure profile. One of the major differences between the profile generated when erosive burning is taken into account and the one when it

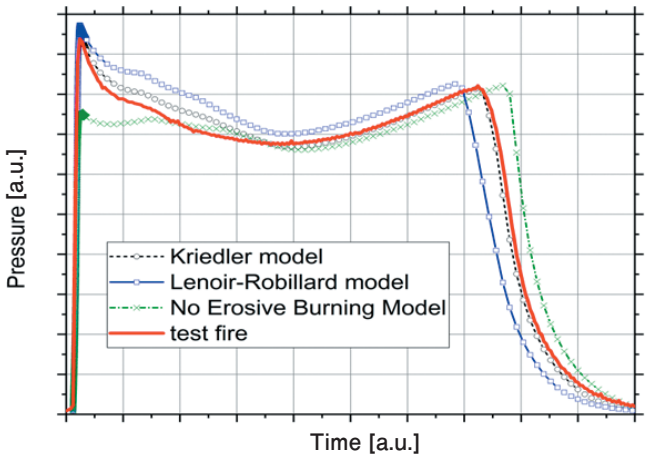

Figure 2 Static test fire results vs. simulation of early highly volume loaded motors at IMI systems.

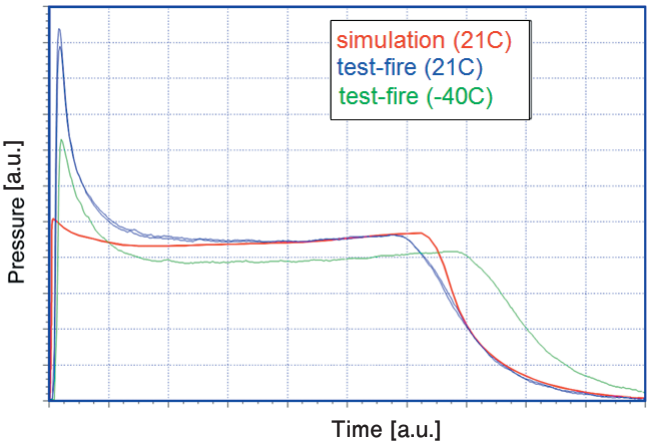

Figure 3 test results (blue) vs. simulated (red) pressure profile of a booster motor. In green is a test fire conducted at low temperature, with lower burning rate.

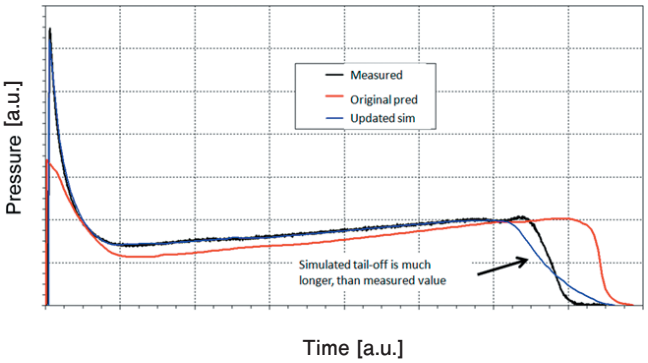

Figure 4 Initial prediction (red), Measured (black) and updated simulation (blue) for a modern rocket motor.

is not, is that the maximum pressure shifts from the beginning to the end of the profile. It is also important to note that while the Lenoir Robillard model gives a good prediction of initial pressure, the pressure during the rest of the profile is higher than the measured value, causing the simulated profile to terminate early compared to the measured results. This will be discussed further on.

Our first encounter with "surprising" results due to erosive burning occurred several years later during the first static test of a small booster, as part of the development program. In Figure 3 the measured and predicted pressure profile can be seen:

In this case the same empirical factors as the previous example where used in Kriedler's model to simulate the pressure profile. It was assumed that since the propellant composition for both motors was similar the same factors should apply. What was not taken into account is that the Vielle law burning rate was different. The booster motor used a slower propellant. This is known to increase sensitivity to erosive burning. Other differences were the dimensions of the motors (the booster being significantly smaller), and the maximum internal flow velocity (the booster having an initial internal Mach number of Mach 0.4 and the larger motor a value of Mach 0.3).

Subsequent modification of the Lenoir Robillard model enabled a reasonable agreement between predicted and measured pressure profiles, and this was implemented during the final development stage of the booster. The Lenoir Robillard model was chosen, because it offered a simple engineering solution to the problem, since it incorporates only two empirical constants. This enables less trial and error until a good fit can be achieved.

The internal ballistics department of IMI systems ensued to develop motors for our modern rockets, using the Lenoir Robillard model. Using data acquired from previous development projects (two of which were described herein), we already anticipated that low burning rates would result in increased sensitivity to erosive burning. For this reason the first static test of our novel rocket system was dedicated, in part, to calibrate the Lenoir Robillard parameters. The results of this test can be seen in Figure 4.

As can be seen, even though a change in erosive burning due to a decrease of burning rate was anticipated, the actual result was much higher than expected. In order to fit the simulation to the test, the erosive burning factor had to be increased by a factor of almost 2. Although a good agreement was achieved during most of the profile, the simulated tail-off was much longer than the measured results. The tail-off occurs when part of the burning front (propellant surface) reaches the motor casing, causing a decrease in burning area. In a perfectly cylindrical motor and case, in which the burning rate is constant along the motor, the tail-off is theoretically instantaneous since all the propellant burns out simultaneously. The fact that the measured profile has a shorter than predicted tail-off, indicates that erosive burning was less pronounced than the model predicts, although the agreement in initial pressure suggests that the model parameters are correct. This inconsistency, and the fact that the empirical constants vary quite drastically between propellants with different burning rates, has led us to work on improving the erosive burning model. To do so, a subscale motor was constructed which enabled us multiple test firing at a low cost. This motor was adequately dubbed Erosive Burning Test Motor (EBTM).

2.3 Erosive burning test motor

Figure 5 depicts the main parts of the test motor. The motor is essentially a pressurized case with adjustable nozzle fittings. The propellant under study is cast into a PVC sleeve, which is then inserted into the casing. The aft dome is fitted with an appropriate nozzle and screwed into the casing. Pressure measurements were taken through the forward dome and the aft dome. The propellant geometry was designed based on the previously described booster. This highly loaded geometry leads to high internal flows. The velocity is determined by the throat area. In a standard set of experiments several tests are performed each time using a different throat diameter. This enabled studying the same propellant composition under different flow conditions (typically Mach 0.2–0.4). The aft and forward pressure measurements enable to determine the pressure differential, thus confirming the flow velocity. Thrust measurements are taken as backup

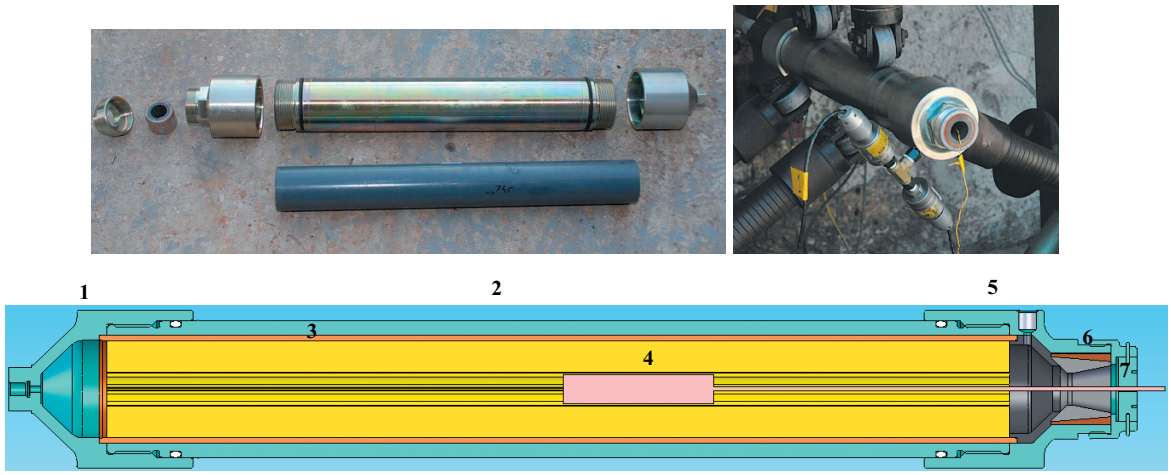

Figure 5 Top left - EBTM parts, Top right - EBTM on test rig. Bottom - CAD model of EBTM: 1 - Forward dome with pressure and thrust gage adapters; 2 - Thick walled steel casing; 3 - Solid propellant cast in removable PVC sleeve; 4 - Matchhead igniter; 5 - Aft dome with pressure gauge adapter; 6 - Nozzle assembly (adjustable throat diameter); 7 - Burst diaphragm.

to pressure results.

A typical pressure profile from this motor can be seen in Figure 6. In Figure 6 the pressure profiles were simulated using Lenoir Robillard model. Constant parameters could not be used to fit both the high (Mach 0.4) and low (Mach 0.2) test results. Instead the parameter β was changed to get a good agreement of initial pressure. It can also be seen that while there is a good agreement between measured and simulated initial pressure the simulated pressure during the rest of the profile is higher than measured results. Consequently, the simulated profile is also shorter and has a longer tail-off. This suggests that while erosive burning is predicted (reasonably) accurately at the initial stage, the simulation predicts a continuation of erosive burning that does not exist in reality. This required an update of the erosive burning model.

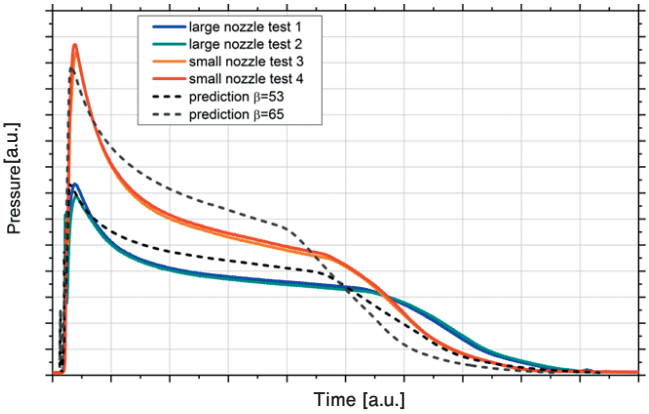

Figure 6 Head pressure profile for different tests of same propellant. Predictions using Lenoir Robillard model do not give adequate agreement between measured and predicted profiles.

2.4 Updating of the erosive burning model

In order to confirm the suspicion that the Lenoir Robillard model causes a residual erosive burning augmentation, even when in reality none should exist, the predicted burning rate of our internal ballistic code was studied for the case of the EBTM, particularly near the end of combustion when the motor port area is large and low flow velocities are expected. The results are summarized in Table 1. As can be seen from Table 1, Lenoir and Robillard's model does indeed predict erosive burning when none should exist. This happens because the basic Lenoir Robillard model does not include a threshold value, which Kriedler and Saderholm model did include.

Table 1 Predicted values of EBTM at end of profile.

Parameter \ Nozzle	small	large
Predicted Mach no.	0.07	0.09
Pressure [kgf cm^{-2}]	53.8	35.7
Burning rate [cm s^{-1}]	0.68	0.59
Vielle burning rate, r_0 [cm s^{-1}]	0.61	0.53
Erosive burning increase	+11%	+10%

In order to avoid this issue, a simple, implementable, yet physically realistic model was needed. The Kriedler model, which does include a threshold condition was already shown to be erratic, requiring constant parameter fitting. Saderholm's model suffered from convergence problems when an attempt was made to integrate it into our code. A quick literary survey was conducted in an effort to find a viable model.

Our survey resulted in a model proposed by Makunda and Paul[9), 10)]. This model had the exact attributes we were seeking, It was physically based, had a threshold condition, and minimal empirical parameters. It is also easily implemented in 1D internal ballistic codes. The mathematical formulation of the model is:

$$\frac{r}{r_0} = 1 + K_1\left(g^{0.8} - g_{th}^{0.8}\right)H\left(g - g_{th}\right)$$
$$g = g_0\left(\mathrm{Re}_0/1000\right)^m \qquad (9)$$
$$g_0 = \frac{G}{r_0 \cdot \rho_p},\ \mathrm{Re}_0 = \frac{\rho_p \cdot r_0 \cdot D}{\mu}$$

(Where K_1 is an empirical factor and g_{th} is the threshold value of the normalized mass flux. H is the Heaviside

function).

Implementation of the functions into our in-house internal ballistics code was done, and empirical data from (9) were used for K_1 and g_{th}. The simulation was tested versus test results from the EBTM. Results of the comparison are presented in Figure 7. The agreement between simulated and measured results is pronounced, especially when compared to the previous model. Both initial pressure and tail-off are accurately predicted, for both flow velocities, without the need to adjust empirical constants.

Encouraged by these results, simulations were performed for several other IMI system motors which exhibit erosive burning. The results of the simulations can be seen in Figure 8. As can be seen, in all cases Makunda and Paul's model gives a better fit to test results than Lenoir Robillard's model, with the added benefit that no adjustment of parameters need be made.

2.5 Conclusion on erosive burning

IMI system has been designing motors with erosive burning for over three decades now. Initially, erosive burning was addressed only experimentally with erosive burning models serving as basic guidelines. Today, IMI systems has developed tools to study and measure erosive burning parameters in a subscale motor dubbed EBTM. The results enabled us to study different models and have improved our understanding of erosive burning. By using this tool, and collecting data from previous test fires it was found that the popular Lenoir Robillard model, although applicable to specific cases after calibration, is not sufficiently universal. In cases were erosive burning is pronounced this model tends to predict erosive burning augmentation when none should exist, and parameters which should be constant cannot be used adequately to predict different conditions.

By applying Makunda and Paul's model to our internal ballistics code, we have found that we can improve our prediction of initial pressure, which is essential in motors in which high erosive burning occurs during ignition. This model also improves prediction throughout motor operation, up to and including the tail-off. Although the parameters reported in the literature fit quite well in most cases to which we applied the model, in some cases slightly alteration of parameter K_1 or g_{th} was required.

3. Ignition delay in motors with aft igniters

3.1 Background

Ignition of a high performance solid motor is a complex process involving the interaction between igniter gases, convective heating of the propellant surface, flame spreading, the developing flow field, and erosive burning[11]. The ignition process can be divided to three consecutive stages: the preheat or induction interval, flame spreading interval, and the chamber filling interval. Figure 9 shows the differences in ignition process between a motor with a high port to throat area ratio and low cross-flows and a motor with high port to throat area ratio with result of high cross-flows over the propellant surface and a dominant erosive burning.

During the induction interval the igniter operates, spreading hot combustion products that heat and start the ignition process of the motor propellant grain. In order to shorten the ignition process and reduce motor to motor variation, the igniter should reach as much propellant surface as possible.

During the second stage, the ignition of the propellant spreads away from the area that was directly ignited by the igniter gases. The flame spreading depends on the evolving flow field, heat transfer to the propellant and the igniter and propellant composition[12]. The heat transfer to the igniting propellant is dominated by several mechanisms: conduction through the propellant, radiation from the spreading flame front, radiation from combustion products in the flow field, and forced convection of hot gases and condensed particles from the flow field. Figure 10 shows the different heat transfer mechanisms that controls the flame spreading.

The low conductivity of the propellant and the perpendicular propellant flame front means that conduction through the propellant and flame front radiation have lower influence than mechanisms of heat transport from the flow field. Therefore, if the igniter is located in the forward end of the motor, the flame

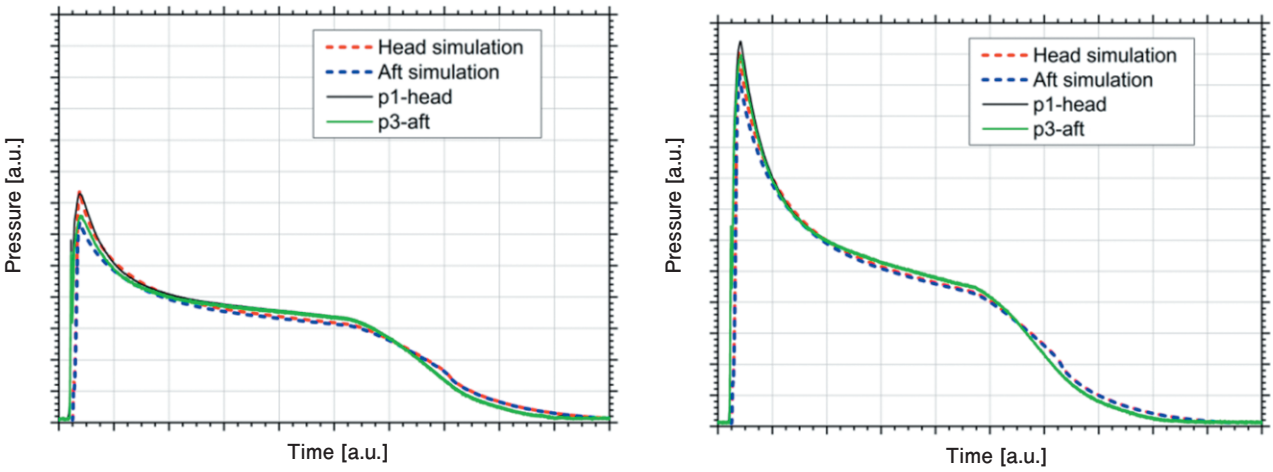

Figure 7 Simulation (dashed) vs. test results (solid) of EBTM using Makunda and Paul model. Left - large nozzle, Right - small nozzle. Parameters from [9] used without adjustment.

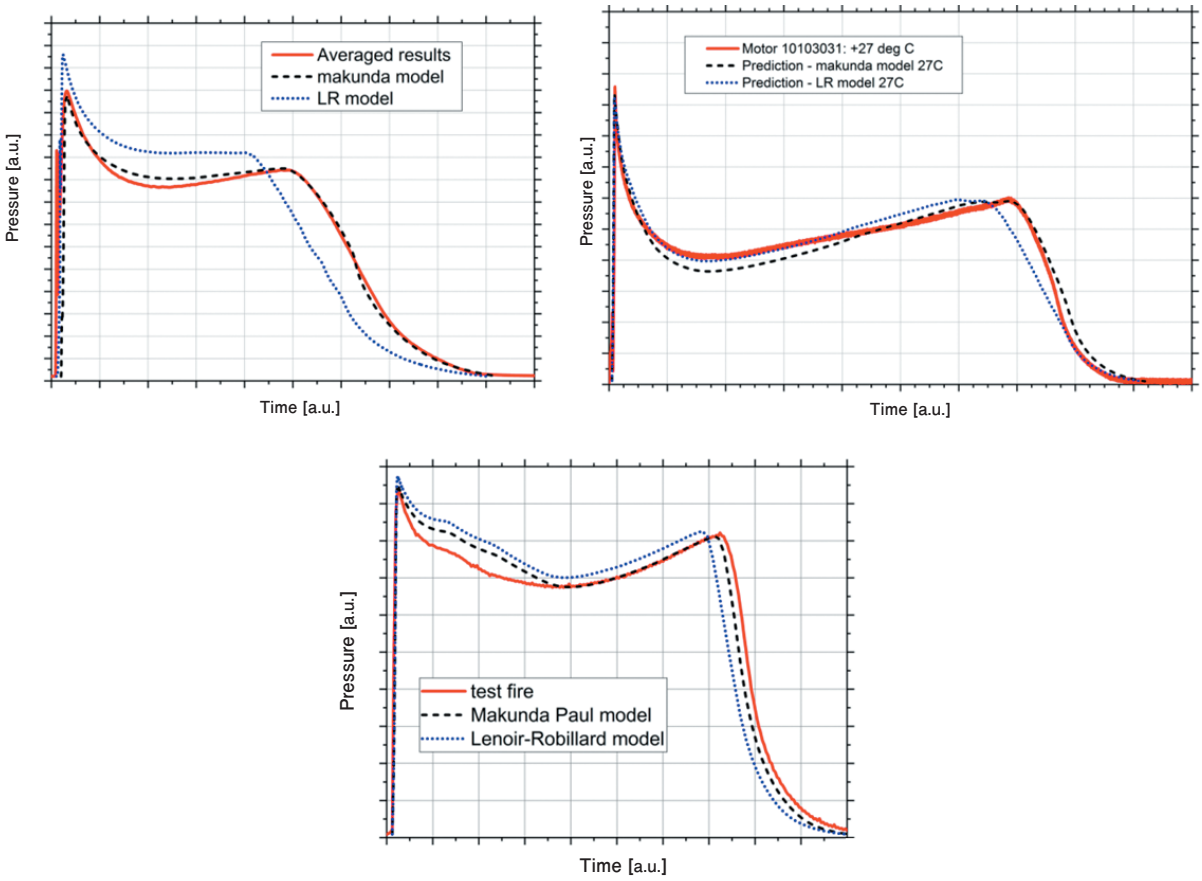

Figure 8 Comparison of test fire results (solid) to predictions using Lenoir Robillard model (parameters fitted for each test) and Makunda Paul model (universal parameters). Top Left: EBTM with slow propellant; Top Right: modern rocket motor; Bottom: old rocket motor.

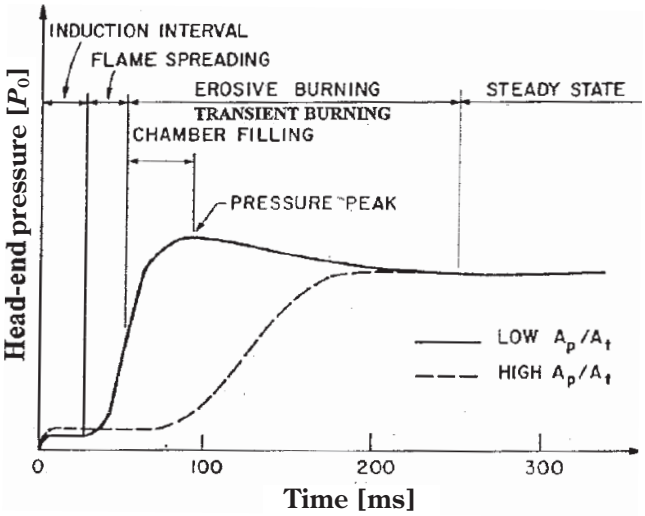

Figure 9 Typical starting transient of motors with low A_p/A_t compared with that of motors having high A_p/A_t [11].

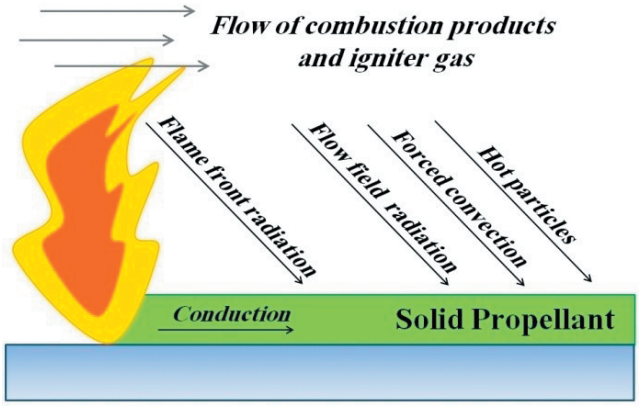

Figure 10 Physical processes involved during flame spreading over solid propellants [13].

spreading is mainly dominated by the flow field convection and radiation. Flame spreading by heat transfer from the flame front happens if the propellant is not exposed to hot gases, as in deep slots and areas that are upstream from the igniter's exposure zone.

During the chamber filling the mass flux from the propellant surface exceeds the mass flux that passes through the nozzle and the motor is pressurized. The rising pressure increases the propellant burning rate and high cross-flow velocities may lead to erosive burning that will form additional increase in burning rate. For a motor with a low port-to throat area ratio the result is a rapid increase in chamber pressure and a shorter starting transient than in high port-to-throat motors.

The most common location for the igniter is in the forward end of the motor, with the exhaust products flowing down the center port. This arrangement provides efficient utilization of energy from the igniter and from ignited portions of the grain because the exhaust flow is over the unignited portion of the propellant. This flow promotes rapid flame propagation and consequently shorter ignition time.

In some instances, igniters are mounted external to the

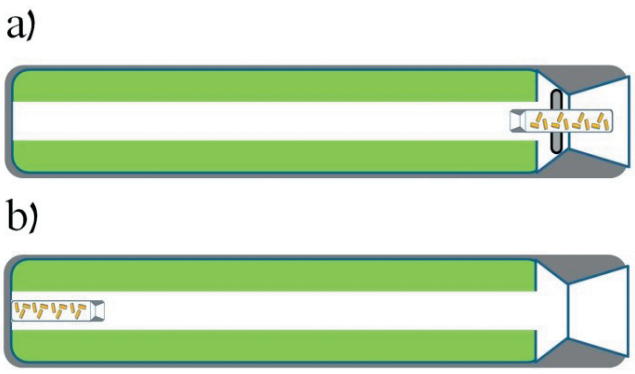

Figure11 A rocket motor with an aft-end igniter (a) and a front-end igniter (b).

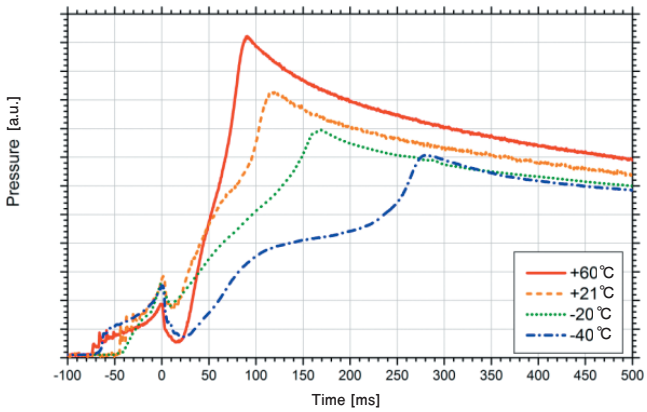

Figure12 Ignition transient of several test fires, using aft igniters, at different temperatures. As the temperature decreases the ignition profile changes to a two step profile.

motor within the nozzle exit cone as presented in Figure 11. The igniter combustion products are spreading forward in the center port, usually with the addition of igniting pellets that serves as additional ignition sources[14]. The pellets, usually compressed boron-potassium-nitrate powder, are initiated in the igniter and ejected into the port in order to expand the propellant area that is affected by the igniter. After ignition, the igniter casing is ejected from the rocket nozzle allowing the free flow of combustion products. In some designs the igniter is fully blocking the nozzle by a diaphragm that seals the motor and enables rapid pressure buildup and improved ignition conditions. The main advantage of an aft-end igniter is the saving in rocket inert mass as the igniter casing is ejected and most of the ignition system (power supply, safe and arm...) can be external to the rocket.

Such is the case for one of our aforementioned motors. A pyrotechnic charge is used to ignite the motor, and is situated within the nozzle assembly. The igniter is held in place by an adapter fitted in the nozzle burst diaphragm. The diaphragm is designed to be ejected once internal motor pressure exceeds a critical value. This value can only be achieved once the motor has begun combustion, thus ensuring high pressure produced by the igniter until motor ignition.

In Figure 12, the ignition pressure profile of several test fires can be seen. Initially, the pressure increases due to combustion of pyrotechnic powder and pellets of the igniter. This occurs while the burst diaphragm is still intact, and the motor is essentially a closed volume system. At a certain time between 30–50 milli-seconds from igniter activation, there occurs an increase in the pressure gradient, indicating additional mass flow due to ignition and combustion of the propellant. When the pressure reaches the yield point of the burst diaphragm, there is a sudden discharge of gas because the mass discharge through the newly created orifice is higher than the mass inflow produced by the burning propellant. The slope and minimum value of this drop is dependent on several factors, the chief being: combustion chamber volume to nozzle throat area ratio, the burning area of the ignited propellant at the time of the burst and the burning rate of the propellant. Since the "dip" in pressure is only to about half of the value of the bursting pressure (and less than 10 bars) we deduced that in this case a substantial amount of the total burning area was already ignited at the time of the burst.

In other cases in which the volume to throat area was considerably lower than this case, we have even experienced a total extinction of the ignited propellant surface, resulting in considerable ignition delay (the propellant eventually reignited, probably due to hot spots produced by the igniter pellets). Such extinction has been tied in the literature to the pressure drop gradient. Pressure gradients in the range of 10^3–10^4 bar s^{-1} have been reported as "dangerous" limits which may result in extinction. However, in our experience, there is no clear connection between the pressure gradient and the extinction phenomena. In the same aforementioned motor we had pressure drops in excess of 10^4 bar s^{-1} which did not result in propellant blow-off, and other cases where the pressure drop was less than 10^3 bar s^{-1}, which resulted in complete extinction of the propellant. It is our assumption that the key factor which defines whether extinction will occur or not during a rapid pressure drop is the amount of burning area ignited compared to the total propellant area during such an occurrence.

In Figure 12 at high temperatures, the profile appears smooth and monotonous. At low temperatures, the profile seems to split into a two-step mechanism, indicating that some of the propellant ignites at a later stage.

This causes a change from predicted values, which leads at low temperatures to lower pressure and thrust than predicted, even when the change of burning rate due to temperature is accounted for.

We asked ourselves, why does this happen? Can we predict it?

3.2 CFD Calculations

We developed a simple model to predict the ignition transient. The model consists of solution of the unsteady RANS equations with a two fluids model and post priory estimation of the temperature for ignition time prediction.

3.2.1 Flow model description

The ignition transient is essentially a mixing problem when the igniter gas is injected into the gas in the

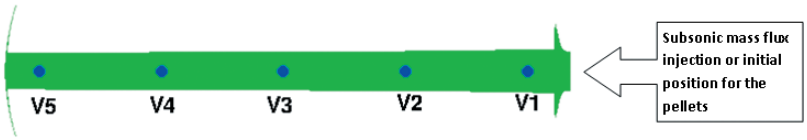

Figure13 Schematic description of the motor and boundary conditions. The enumerated points used for surface temperature evaluation.

chamber (air, mostly). For this reason, we implement in our inhouse code, FLDYNS, a two fluid model which is used for simple simulations of compressible, mixing problems. In this model, the continuity equation replaced by two continuity equations for the two gases:

$$\begin{aligned}\frac{\partial \rho_\alpha}{\partial t}+\nabla(\rho_\alpha \vec{u})&=\nabla\left[\left(\frac{\mu}{Sc}+\frac{\mu_t}{Sc_t}\right)\nabla\frac{\rho_\alpha}{\rho}\right]+\dot{\rho}_\alpha\\ \frac{\partial \rho_\beta}{\partial t}+\nabla(\rho_\beta \vec{u})&=\nabla\left[\left(\frac{\mu}{Sc}+\frac{\mu_t}{Sc_t}\right)\nabla\frac{\rho_\beta}{\rho}\right]+\dot{\rho}_\beta\end{aligned} \tag{10}$$

Where μ and μ_1 are the laminar and turbulent viscosities, Sc and Sc_t are the laminar and turbulent Schmidt numbers. The other Navier-Stokes equations for the momentum and energy are

$$\begin{aligned}&\frac{\partial \rho u\vec{u}}{\partial t}+\nabla\vec{u}(\rho u+p\hat{x})=\nabla\vec{\tau}_x\\ &\frac{\partial \rho v\vec{u}}{\partial t}+\nabla\vec{u}(\rho v+p\hat{y})=\nabla\vec{\tau}_y\\ &\frac{\partial \rho w\vec{u}}{\partial t}+\nabla\vec{u}(\rho w+p\hat{z})=\nabla\vec{\tau}_z\\ &\frac{\partial \rho E}{\partial t}+\nabla(\vec{u}(\rho H)-\nabla(kT))\\ &=\frac{\partial}{\partial x}(\vec{u}\vec{\tau}_x)+\frac{\partial}{\partial y}(\vec{u}\vec{\tau}_y)+\frac{\partial}{\partial z}(\vec{u}\vec{\tau}_z)+\dot{h}\end{aligned} \tag{11}$$

Where $\vec{\tau}_{x,y,z}$ are the stress vectors. The specific energy, ρE, and total enthalpy, ρH, are related to the pressure and the velocity by

$$\rho E=\frac{p}{\gamma-1}+\frac{1}{2}\rho|\vec{u}|^2 \tag{12}$$

$$\rho H=\rho E+p \tag{13}$$

The specific heat capacities and the heat capacity ratio are given by

$$\begin{aligned}C_p&=\frac{y_\alpha}{w_\alpha}\frac{\gamma_\alpha}{\gamma_\alpha-1}+\frac{y_\beta}{w_\beta}\frac{\gamma_\beta}{\gamma_\beta-1}\\ C_v&=\frac{y_\alpha}{w_\alpha}\frac{1}{\gamma_\alpha-1}+\frac{y_\beta}{w_\beta}\frac{1}{\gamma_\beta-1}\\ \gamma&=\frac{C_p}{C_v}\end{aligned} \tag{14}$$

Where y_i, γ_i, w_i with $i=\alpha,\beta$ are the mass fraction, heat capacities ratio and molecular weight of the phase i. the total density and mean molecular weights are

$$\rho=\rho_\alpha+\rho_\beta\quad W^{-1}=\frac{y_\alpha}{w_\alpha}+\frac{y_\beta}{w_\beta}. \tag{15}$$

and the equation of state is

$$p=\frac{\rho RT}{W} \tag{16}$$

3.2.2 Burning rate model from igniter pellets

Igniter pellets are assumed spherical. The burning rate model for igniter pellets is a Vielle type power law in pressure and is given by $r=ap^n$. The total mass flow rate from the pellets is given by $\dot{m}_{tot}=4\pi R^2\rho_P rN$.

Where ρ_p is the bulk density of the igniter charge, and N is the number of pellets:

$$N=\frac{3m_0}{4\pi R_0^3\rho_p} \tag{17}$$

Where m_0 is the initial total mass of pellets and R_0 is the initial radius of each pellet.

A schematic description of an approximated motor geometry and the boundary conditions are presented in Figure 13.

We have implemented gas injections of pellets as a flux injection from the throat area assuming that the pellets are a static "package" of pellets. In this case, the a subsonic inflow boundary condition forced from the throat area with $\rho u=m_{tot}/A_t$, $T=T_{inj}$

3.2.3 Estimation of surface temperature

We now describe a post-processing estimation of the surface temperature of the propellant along the motor. Consider the heat equation in semi-infinite domain

$$\frac{\partial T}{\partial t}=\alpha\frac{\partial^2 T}{\partial x^2}$$

where $x\in[0,\infty)$ with the boundary conditions (18)

$$k\frac{\partial T}{\partial x}(0,t)=-q(t)$$

and initial condition

$$T(x,0)=T_{amb}$$

where α is the thermal diffusivity and k is the thermal conductivity.

The surface temperature is given by

$$T_s(t)=T(0,t)=T_{amb}+\sqrt{\frac{\alpha}{\pi}}\int_0^t\frac{q(\tau,T_s)}{k}\frac{d\tau}{\sqrt{t-\tau}} \tag{19}$$

Equation (19) is an integral equation and can be solved using iterative methods (for example, using Neumann series).

The heat flux is given by:

$$q(t,T_s)=h\cdot(T_r-T_s)+\varepsilon\sigma\left(T_f^4-T_s^4\right) \tag{20}$$

The heat transfer coefficient, h, is calculated using the fluid properties and flow condition at the center line of the motor

$$h=0.023(\rho u)^{4/5}\mathrm{Pr}^{-7/10}\left(\frac{\mu}{D}\right)^{1/5}\frac{\gamma}{\gamma-1}\frac{R}{W}$$

Where D is the effective diameter, Pr is the Prandtl number of the gas, μ is the viscosity. γ and W are the heat capacity ratio and the mean molecular weight. Also in Equation (20), T_f is the gas temperature and T_r is the recovery temperature, given by

$$T_r = T_f\left(1+\frac{\gamma-1}{2}M^2\right)$$

where M is the Mach number. The emissivity of combustion gases was estimated using the work of Chang et al.[15)]

3.2.4 Results

The surface temperature was evaluated in five points along the surface. The points can be seen in Figure 13. For 32 g and 65 g igniter charge, the surface temperature as a function of time is presented in Figures 14 and 15, respectively. It can be seen that the temperature in the two last points close to the motor head rise considerably slower than the rest. Similar phenomena were reported by Cho et al.[16)] Temperature contour maps in times up to 0.4 sec are presented in Figure 16.

This happens because of a "syringe" effect. The hot gas moving from the igniter towards the head of the motor is blocked by stagnant cold air. While pressure is readily transferred between the two fluids, the temperature is "trapped" in the rear section and cannot penetrate the head section because the only heat transfer mechanism is diffusion. As a result, only the aft section of the motor ignites, causing an additional pressure rise which leads to bursting of the nozzle diaphragm and ejection of the spent igniter. At this point chocked flow conditions exist and the motor begins to produce thrust. However the propellant surface did not entirely ignite, and so the steady state pressure is lower than that achieved when all the propellant is ignited. Since the head end of the propellant did not ignite, additional time is required for the entire propellant to ignite, since the flame must travel against the flow.

In the simulation, the time when the first point raises above a critical temperature of 815 K is considered to be the ignition time. This time is marked on the pressure curve in Figure 17.

3.3 Conclusion on aft ignition

After analysing much of our experimental data, and running CFD simulations to verify our observations we come to the following conclusions:

1. When firing an igniter in a long, closed motor, some of the surface ignites with a delay due to the fact that hot gases do not penetrate into the cold air stored in the motor port.

2. In the case of aft ignition, after nozzle diaphragm bursts and flow ensues, flame spreading towards motor head is hindered.

3. The phenomenon is more substantial at low, sub-zero, temperatures than ambient temperatures due to increased difficulty to ignite the propellant. This may be due to propellant frosting.

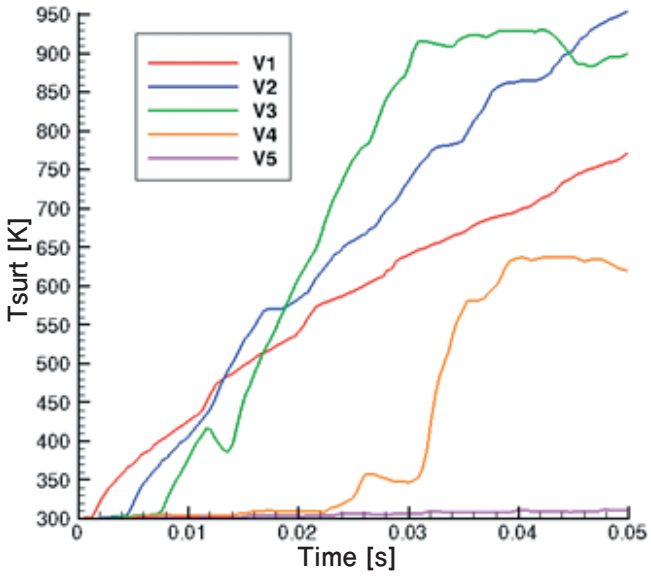

Figure14 Predicted surface temperature at different points along the propellant, 32 grams ignition charge.

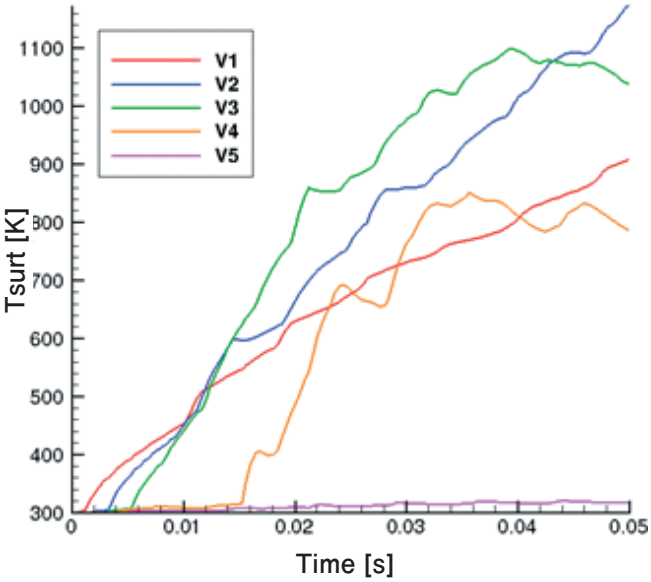

Figure15 Predicted surface temperature at different points along the propellant, 65 grams ignition charge.

4. Conclusion

It was shown that transient phenomena have a significant impact on motor thrust profile, specifically during and near ignition. Due to the sensitivity of mission success on the motor thrust profile, IMI systems has conducted extensive research aimed at better understanding and reducing uncertainties during this stage. It is our belief that two major transient processes control the motor pressure profile during ignition: propellant ignition and erosive burning.

Propellant ignition, although comprehensively studied, is not yet clearly understood. This is probably due to the fact that the physical and chemical processes leading to ignition are numerous and complex, and cannot easily be resolved experimentally. Up to date, all attempts at constructing a "simplified" ignition theory has been only partially successful. From a system engineering point of view, the tricky nature of ignition has often led to

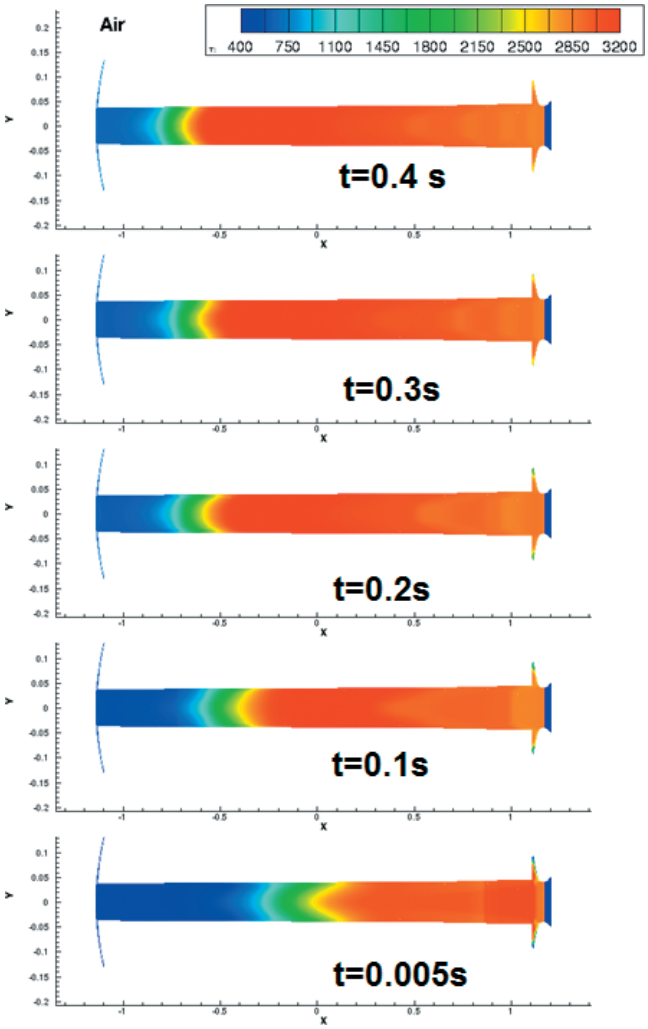

Figure16 Internal flow field temperature contour map at different times.

surprises during development phases. Systems which we had believed to be well characterised, turned out to produce over or under-spec results, forcing redesign of the ignition system. From every such occurrence, we have learnt a little bit more about the nature of ignition.

Erosive burning was a rare (yet expected) phenomenon at IMI systems about three decades ago. Since then, our motors have become increasingly loaded, resulting in motors with high internal flow velocities, causing considerable erosive burning. We have dealt with the phenomena initially empirically, using a trial and error experimental approach. With time, our simulation methods improved enough to employ complex burning rate mechanism. Today, we can predict erosive burning pressure overshoot with high certainty (about 5%), even before the first static test, by employing specifically designed small ballistic evaluation motors, and a very sound mathematical model in our ballistic code.

IMI systems employs powerful tools to elucidate transient phenomena, when designing our motors. We have learnt to identify factors contributing to poor ignition, such as rear igniters employing a mixture of pyrotechnic powder and pellets, and are even able to simulate the effects caused by them. We have improved our ballistic code to account for erosive burning based on

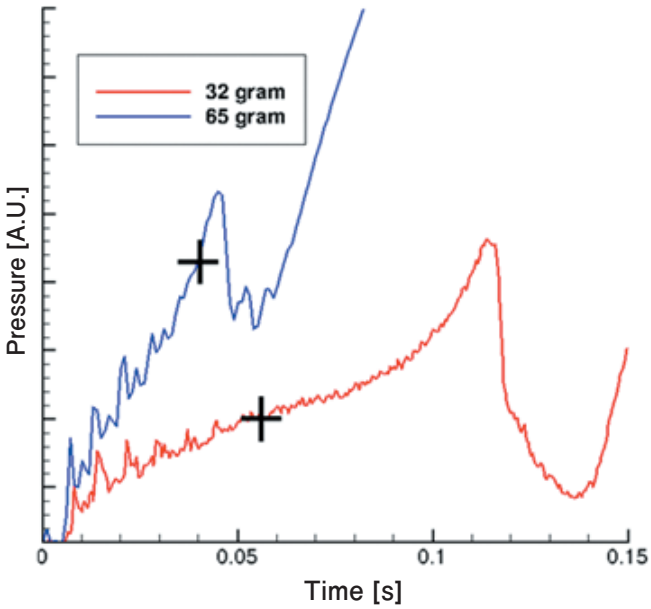

Figure17 pressure as function of time. The evaluated ignition time is marked with black "plus" signs.

contemporary theories, and have bench marked our code using carefully designed experiments, as well as checking existing and new experimental data obtained from static tests. The field of transient phenomena is always exciting and difficult to simulate: it is our hope that by sharing our insights, we can all benefit from the collective knowledge acquired over the years.

References

1) G.P. Sutton and D.M. Ross, "Rocket Propulsion Elements, 4th ed.", 7–10, John Wiley & Sons, New York, USA (1976).
2) F.A. Williams, M. Barrere, and N.C. Huang, "Fundamental Aspects of Solid Propellant Rockets", 60–61, Technivision Services, Slough, England (1969).
3) M.K. Razden and K.K. Kuo, "Fundamentals of Solid–Propellant Combustion, Progress in Astronautics and Aeronautics", Chapter 10: "Erosive Burning of Solid Propellants", 90 (1984).
4) L. Green, Jet Propulsion, 24 (1954).
5) E.M.Landsbaum, Journal of Propulsion and Power, 21, 470–477 (2005).
6) J.W. Kreidler, AIAA Solid Propellant Rocket Conference, Palo Alto, California, AIAA no. 64–155 (1964).
7) C.A. Saderholm, AIAA Paper, 72–1145 (1972).
8) J. M. Lenoir and G, Robillard, Proc. Sixth Symposium (International) on Combustion, 6, 663–667 (1957).
9) H.S. Mukunda and P. J. Paul Combust. Flame, 109, 224–236 (1997).
10) H.S. Mukunda, P.J. Paul, A. Javed, and D. Chakraborty, Acta Astronautica, 93, 176–181 (2015).
11) A. Peretz, K.K. Kuo, L.H. Caveny, and M. Summerfield., AIAA Journal, 11, 1719–1727, doi.org/10.2514/3.50676 (1973).
12) V.R. Sanal Kumar and B. N. Raghunandan, 48th AIAA/ASME/SAE/ASEE Joint Propulsion Conference & Exhibit, Atlanta, USA, 30 July1–Aug. 2012, Paper No. AIAA 2012–4043 (2012).
13) K. K. Kuo and M. Summerfield, "Fundamental aspects of solid propellant rockets", Progress in Astronautics and

Aeronautics, AIAA, Vol.90, (1982).
14) D. R. J. Greatrix, J. Gottlieb, and T. Constantinou, Journal of Propulsion and Power, 4, 412−420, doi.org/10.2514/3.23082 (1988).
15) S. T. Chang, S. Han, and J. C. Chai, AIAA paper, 96-3055. (1996).
16) I. H. Cho and S. W. Baek, Combust. Sci. Technol., 152, 81−98 (2000).